Article

Exploring Global Polarization Splitting in Au+Au Collisions at $\sqrt{s_{\mathrm{NN}}} = 19.6$ GeV Using Viscous Hydrodynamic Model CLVisc

Shasha Ye, Xuefei Yuan and Zefang Jiang

Article

Exploring Global Polarization Splitting in Au+Au Collisions at $\sqrt{s_{\mathrm{NN}}}$ = 19.6 GeV Using Viscous Hydrodynamic Model CLVisc

Shasha Ye [1,†], **Xuefei Yuan** [1,†] **and Zefang Jiang** [1,2,*]

1   Department of Physics and Electronic-Information Engineering, Hubei Engineering University, Xiaogan 432000, China

2   Key Laboratory of Quark and Lepton Physics (MOE), Institute of Particle Physics, Central China Normal University, Wuhan 430079, China

*   Correspondence: jiangzf@mails.ccnu.edu.cn

†   These authors contributed equally to this work.

Abstract: We present a systematic study of the global polarization of Λ and $\bar{\Lambda}$ hyperons in Au+Au collisions at $\sqrt{s_{\mathrm{NN}}}$ = 19.6 GeV using the viscous hydrodynamic model CCNU-LBNL-Viscous hydrodynamic model (CLVisc) with a modified 3D optical Glauber model initial condition. The global polarization splitting as a function of transverse momentum and rapidity is investigated. It is shown that the magnitude of the net baryon density and its longitudinal titled geometry at the initial stage both have significant effects on the global polarization splitting of Λ and $\bar{\Lambda}$ hyperons. Specifically, an increase in the magnitude of the net baryon density leads to a corresponding minor increase in the global polarization splitting. Similarly, alterations in the tilted geometry of net baryon density results in significant changes in the splitting of the global polarization.

Keywords: global polarization splitting; $\Lambda/\bar{\Lambda}$ hyperons; hydrodynamic model CLVisc; finite net baryon density

1. Introduction

Under normal conditions, quarks and gluons exist as bound states to form hadrons. However, under extreme conditions, such as energy densities ≥ 1 GeV/fm^3, they become deconfined and form a highly excited state of nuclear matter known as the quark–gluon plasma (QGP) [1–8]. This state is believed to be a key component of the universe's very early stages. The study of QGP is important for understanding the properties of strongly coupled matter and for searching for the existence of a phase transition from hadronic matter to QCD matter, which provides insights into the formation of galaxies and the evolution of the universe [9]. Currently, the QGP can be produced in laboratory by the Relativistic Heavy Ion Collider (RHIC) and the Large Hadron Collider (LHC).

In a typical non-central nucleus–nucleus collisions, large orbital angular momentum (OAM) is created. This large OAM can induce the polarization of hyperons through the spin-vorticity coupling [10,11] or spin-orbital coupling [12–17]. Recently, the global polarization of $\Lambda(\bar{\Lambda})$ hyperons has been successfully observed by STAR Collaboration in 7.7–200 GeV semi-peripheral Au+Au collisions at RHIC [18–20]. It is found that the average fluid vorticity achieves $\omega \approx (9 \pm 1) \times 10^{21}$ s^{-1}. This is the fastest vortical system ever created in laboratory and observed in nature to date. Further studies of the global and local polarization have provided new insights into the vortical properties of QGP at high energy. Extensive theoretical and phenomenological studies have been devoted to the influence of vorticity on spin polarization in QGP, including 3+1 D hydrodynamic framework [21–28] and multistage transport approach [29–32]. These models all provide good descriptions of the global polarization at RHIC and LHC. However, theoretical calculations have yielded an opposite sign of azimuthal-angle dependence compared to the measured data of polarization. Besides the global polarization of $\Lambda/\bar{\Lambda}$, the spin polarization

can also lead to other effects and observables, such as spin alignment [33] and baryonic spin hall effect [28,34,35].

In this work, following our previous works [36,37], we perform a study on the Λ and $\bar{\Lambda}$ global polarization in 19.6 GeV Au+Au collisions, using the viscous hydrodynamic model CLVisc [38] with a modified 3D optical Glauber model initial condition. Such hydrodynamic models and hybrid approaches have been widely used to simulate the nucleus–nucleus collisions at RHIC and the LHC energies, which successfully describe many final state observables such as multiplicity distribution, transverse momentum distribution, collective flow and spin polarization [24,28,39–43]. Despite numerous studies on hyperon polarization using hydrodynamic models, the cause of the splitting in the global polarization of Λ and $\bar{\Lambda}$ hyperons remains an open question. While in Refs. [21,31,44,45], it has been suggested that this behaviour can be related to the net baryon density or the strong electromagnetic field, detailed analysis is still lacking. In this study, we will further study the global spin polarization within the CLVisc hydrodynamic model with finite net baryon density, which nicely describes the measured centrality, rapidity and transverse momentum dependence of $\Lambda/\bar{\Lambda}$ global polarization in 19.6 GeV Au+Au collisions. In order to study the splitting of the spin polarization, we focus on investigating the impact of the magnitude of net baryon density and its tilted geometry on the splitting of hyperons global polarization along the out-of-plane direction ($-P^y_{(\Lambda-\bar{\Lambda})}$).

The paper is organized as follows. Section 2 gives a brief description of the 3D optical Glauber model, hydrodynamic model CLVisc and the spin polarization formula in this work. The impact of the baryon density on the hyperons global polarization splitting is studied in Section 3. Section 4 concludes and summarizes this paper.

2. Model Framework

2.1. Initial Condition: Modified 3D Optical Glauber Model

We employ a longitudinal tilted initial conditions developed in Refs. [36,37] to generate initial conditions for the QGP hydrodynamic simulation. Based on the Wood–Saxon distribution, the nuclear thickness function is given by

$$T(x,y) = \int_{-\infty}^{+\infty} dz \frac{\rho_0}{1 + e^{(\sqrt{x^2+y^2+z^2}-R_0)/d_0}}. \tag{1}$$

Here, ρ_0 is the average nuelcon density, (x,y,z) are the spatial coordinates, R_0 is the nuclear radius, and d_0 is the surface diffusiveness parameter. For ^{197}Au nucleus in this study, we selected $\rho_0 = 0.17$ fm^{-3}, $R = 6.38$ fm, $d = 0.535$ fm. When two nuclei move along the $\pm \hat{z}$ direction and collide with impact parameter $\mathbf{b}$, their thickness function is

$$T_+(x_\mathrm{T}) = T(x_\mathrm{T} - \mathbf{b}/2), \quad T_-(x_\mathrm{T}) = T(x_\mathrm{T} + \mathbf{b}/2), \tag{2}$$

where $x_\mathrm{T} = (x,y)$ is the transverse plane coordinate. Based on the standard optical Glauber model, the density distribution of participating nucleons in the projectile and target nucleus is

$$T_1(x_\mathrm{T}) = T_+(x_\mathrm{T})\left\{1 - \left[1 - \frac{\sigma_\mathrm{NN} T_-(x_\mathrm{T})}{197}\right]^{197}\right\},$$
$$T_2(x_\mathrm{T}) = T_-(x_\mathrm{T})\left\{1 - \left[1 - \frac{\sigma_\mathrm{NN} T_+(x_\mathrm{T})}{197}\right]^{197}\right\}. \tag{3}$$

Here, σ_NN is the cross-section of inelastic scattering between nucleons [46]. Following our earlier studies [47–49], the wounded (or participant) nucleon distribution is

$$W_\mathrm{N}(x,y,\eta_\mathrm{s}) = T_1(x,y) + T_2(x,y) + H_\mathrm{t}[T_1(x,y) - T_2(x,y)] \tan\left(\frac{\eta_\mathrm{s}}{\eta_\mathrm{t}}\right), \tag{4}$$

where H_t reflects the overall strength of the medium's tilt deformation relative to the longitudinal direction. It is a function of the impact parameter. By fitting the directed flow experimental data from various centrality classes in 19.6 GeV Au+Au collisions, we parametrize $H_t = 2.2b/\text{fm}$ [36]. Additionally, $\tan\left(\frac{\eta_s}{\eta_t}\right)$ controls the slope of the initial energy density in the direction of beam rapidity, where $\eta_s = \frac{1}{2}\ln\frac{t+z}{t-z}$ represents the spacetime rapidity. For all collision systems, we set η_t to be 8.0. This leads to a counterclockwise tilted geometry of the QGP fireball [50,51] in the reaction plane with respect to the beam direction [47].

The total weight function encompassing both wounded (participant) nucleons and binary (hard) collisions is

$$W(x,y,\eta_s) = \frac{0.95 W_N(x,y,\eta_s) + 0.05 n_{BC}(x,y)}{[0.95 W_N(0,0,0) + 0.05 n_{BC}(0,0)]|_{\mathbf{b}=0}}, \tag{5}$$

where 0.05 is the collision hardness parameter [39,52], which is determined by the centrality dependence of the soft hadron yield. The number of binary collisions $n_{BC} = \sigma_{NN} T_+(x,y) T_-(x,y)$ [39,46]. The initial energy density and local baryon density can be obtained in terms of the Bjorken flow, as follows [39,41]:

$$\varepsilon_0(x,y,\eta_s) = K \cdot W(x,y,\eta_s) \cdot H(\eta_s), \tag{6}$$

$$n_0(x,y,\eta_s) = \frac{1}{N} \cdot W(x,y,\eta_s) \cdot H(\eta_s) \cdot H_B(\eta_s), \tag{7}$$

where K is an overall factor that is constrained by the multiplicity distribution ($dN_{ch}/d\eta$ or dN_{ch}/dy), and N is a normalization factor [53,54].

Following Refs. [36,51,52], we used the $H(\eta_s)$ function (an empirical formula) to satisfy the plateau structure of $dN/d\eta$ for charged hadrons in the most central region:

$$H(\eta_s) = \exp\left[-\frac{(|\eta_s| - \eta_\omega)^2}{2\sigma_\eta^2}\theta(|\eta_s| - \eta_\omega)\right], \tag{8}$$

where η_ω is the width of the platform at the middle rapidity, and σ_η is the width of the Gaussian decay outside the platform region [36]. Based on the research of Refs. ([36,54]), the longitudinal distribution of the initial local baryons density is given by

$$H_B(\eta_s) = \exp\left[-\frac{(\eta_s - \eta_n)^2}{2\sigma_n^2}\right] + \exp\left[-\frac{(\eta_s + \eta_n)^2}{2\sigma_n^2}\right], \tag{9}$$

where η_n and σ_n can be calibrated using the transverse momentum distribution of identified particles measured in experiments [25,41]. It is worth noting that although this baryon density distribution is a phenomenological model [54], it shares similar qualitative features with the longitudinal distribution given by the string fragmentation model [41,55,56].

This is because the spin polarization is not only sensitive to the QGP geometric shape, but also to the initial flow velocity field of the QGP medium. Following Refs. [25,27,57,58], the initial energy-momentum current is given by

$$T^{\tau\tau} = \varepsilon_0(x,y,\eta_s)\cosh(y_L), \tag{10}$$

$$T^{\tau\eta_s} = \frac{1}{\tau_0}\varepsilon_0(x,y,\eta_s)\sinh(y_L), \tag{11}$$

where $y_L = f_v y_{CM}$, the central-of-mass rapidity $y_{CM} = \text{arctanh}\left[\frac{T_1 - T_2}{T_1 + T_2}\tanh(y_{beam})\right]$, $y_{beam} = \text{arccosh}\left[\sqrt{s_{NN}}/(2m_N)\right]$ and m_N denotes the nucleon mass. The free parameter $f_v \in [0,1]$ controls the longitudinal flow velocity gradient. When $f_v = 0$, one recovers the Bjorken flow scenario. In this work, f_v is set to 0.15 [25,36]. We do not consider the

initial velocity of QGP in the transverse plane at the initial proper time τ_0; thus, $T^{\tau x}$ and $T^{\tau y}$ are both assumed to be zero at $\tau = \tau_0$.

With above initial condition settings, Figure 1 shows the distribution of the initial energy density (left plane) and local (net) baryon density (right plane) on the $\eta_s - x$ plane for 10–40% centrality class Au+Au collisions at $\sqrt{s_{NN}} = 19.6$ GeV. Their values are derived from Equations (10) and (11). One may clearly find that both the energy density and local baryon density exhibit a counterclockwise tilted geometry with respect to the longitudinal (beam) direction. The net baryon density shows a more pronounced shift towards large rapidity and a greater tilt compared to the energy density. This can be explained using the string models of the initial state [55,56,59]: while the baryon density deposition is mainly caused by the valence quarks from the participating nucleons, the energy density deposition arises from the melting of strings that involve both valence and sea quarks.
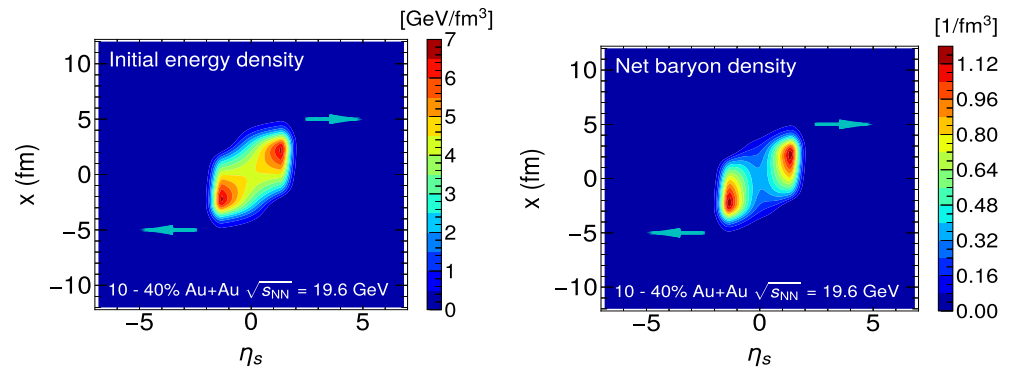
Figure 1. (Color online) Distribution of the initial energy density (**left**) and net baryon density (**right**) on the η_s-x plane for 10–40% Au+Au collisions at $\sqrt{s_{NN}} = 19.6$ GeV. The arrows (cyan color) sketch propagation towards the forward and backward rapidity directions.

2.2. (3+1)D Hydrodynamic Evolution: CLVisc

In this work, we use the (3+1)-dimensional relativistic viscous hydrodynamic model CLVisc [39,41] to simulate the evolution of the system's energy, momentum and net baryon density,

$$\nabla_\mu T^{\mu\nu} = 0, \tag{12}$$

$$\nabla_\mu J_B^\mu = 0, \tag{13}$$

where the energy-momentum tensor $T^{\mu\nu}$ and the net baryon current J_B^μ are given by

$$
\begin{aligned}
T^{\mu\nu} &= \varepsilon U^\mu U^\nu - P\Delta^{\mu\nu} + \pi^{\mu\nu}, \\
J_B^\mu &= n U^\mu + V^\mu,
\end{aligned}
\tag{14}
$$

where ε is the local energy density, U^μ is the flow velocity field, P is the pressure, $\pi^{\mu\nu}$ is the shear viscosity tensor, n is the net baryon density, and V^μ is the baryon diffusion current. The spatial projection tensor is defined as $\Delta^{\mu\nu} = g^{\mu\nu} - U^\mu U^\nu$. In this study, we follow the approaches of Refs. [41,53,55,57,60] and consider only the shear viscosity effect, leaving the impact of bulk viscosity for future investigation. Hydrodynamic equations are solved using a lattice QCD-based Equation of State (EoS) at finite baryon density, known as NEOS-BQS [a QCD equation of state model (NEOS) with multiple charges: net baryon (B), strangeness (S) and electric charge (Q)] [61,62]. This EoS provides a smooth crossover between the QGP and the hadron phase under strangeness neutrality and electric charge density $n_Q = 0.4 n_B$.

As the system evolves below the switching energy density ($e_{frz} = 0.4$ GeV/fm^3), we use the Cooper–Frye formalism to obtain the hardon momentum distribution [36]. We take into account the resonance decay contributions, as performed in Ref. [39], when calculating

the yields and anisotropic flow observables for identified particles. However, the Λ spin polarization is still computed directly on the freeze-out hypersurface, as discussed in the next subsection, without contributions from these resonance decays. Effects of hadronic scatterings after the QGP phase have not been included in this study.

2.3. Spin Polarization of Hyperons

In non-central heavy-ion collisions, a huge initial orbital angular momentum is produced, the presence of fluid vorticity polarizes the spin of fermions through the spin-orbital coupling or spin-vorticity coupling [12,14]. Based on Refs. [63,64], the spin polarization pseudo-vector at thermal equilibrium can be obtained from the modified Cooper–Frye formalism, as follows:

$$\mathcal{S}^\mu(\mathbf{p}) = \frac{\int d\Sigma \cdot p \, \mathcal{J}_5^\mu(p, X)}{2m \int d\Sigma \cdot \mathcal{N}(p, X)}. \tag{15}$$

Here, m is the mass of fermions. The $d\Sigma_\mu$ is the hypersurface element determined by the projection method. The $\mathcal{J}_5^\mu$ is the axial charge current density. The $\mathcal{N}^\mu(p, X)$ is the number density of fermions in the phase space. According to the decomposition of the vector product between the thermal vorticity tensor and the four-momentum vector [65] or the quantum kinetic theory [26,66,67], $\mathcal{S}^\mu(\mathbf{p})$ can be decomposed into several sources:

$$\mathcal{S}^\mu(\mathbf{p}) = \mathcal{S}^\mu_{\text{thermal}}(\mathbf{p}) + \mathcal{S}^\mu_{\text{shear}}(\mathbf{p}) + \mathcal{S}^\mu_{\text{accT}}(\mathbf{p}) + \mathcal{S}^\mu_{\text{chemical}}(\mathbf{p}) + \mathcal{S}^\mu_{\text{EB}}(\mathbf{p}), \tag{16}$$

where

$$\mathcal{S}^\mu_{\text{thermal}}(\mathbf{p}) = \int d\Sigma^\sigma F_\sigma \epsilon^{\mu\nu\alpha\beta} p_\nu \partial_\alpha \frac{u_\beta}{T},$$

$$\mathcal{S}^\mu_{\text{shear}}(\mathbf{p}) = \int d\Sigma^\sigma F_\sigma \frac{\epsilon^{\mu\nu\alpha\beta} p_\nu u_\beta}{(u \cdot p)T} p^\rho (\partial_\rho u_\alpha + \partial_\alpha u_\rho - u_\rho D u_\alpha),$$

$$\mathcal{S}^\mu_{\text{accT}}(\mathbf{p}) = -\int d\Sigma^\sigma F_\sigma \frac{\epsilon^{\mu\nu\alpha\beta} p_\nu u_\alpha}{T} \left(D u_\beta - \frac{\partial_\beta T}{T} \right),$$

$$\mathcal{S}^\mu_{\text{chemical}}(\mathbf{p}) = 2\int d\Sigma^\sigma F_\sigma \frac{1}{(u \cdot p)} \epsilon^{\mu\nu\alpha\beta} p_\alpha u_\beta \partial_\nu \frac{\mu}{T},$$

$$\mathcal{S}^\mu_{\text{EB}}(\mathbf{p}) = 2\int d\Sigma^\sigma F_\sigma \left[\frac{\epsilon^{\mu\nu\alpha\beta} p_\alpha u_\beta E_\nu}{(u \cdot p)T} + \frac{B^\mu}{T} \right], \tag{17}$$

where

$$F^\mu = \frac{\hbar}{8 m_\Lambda \Phi(\mathbf{p})} p^\mu f_{\text{eq}} (1 - f_{\text{eq}}),$$

$$\Phi(\mathbf{p}) = \int d\Sigma^\mu p_\mu f_{\text{eq}}, \tag{18}$$

where the thermal distribution $f_{\text{eq}} = \frac{1}{\exp[(p_\mu U^\mu - B\mu_B)/T_f] \mp 1}$. Here, μ_B is the net baryon chemical potential, B is the baryon number for the identified baryon, T_f is the chemical freeze-out temperature. Since the net baryon density is not zero, the value of μ_B and T_f are different for each hypersurface cell [41]. The above equation represents the thermal vorticity polarization vector ($\mathcal{S}^\mu_{\text{thermal}}$), shear tensor polarization vector ($\mathcal{S}^\mu_{\text{shear}}$), fluid acceleration minus temperature gradient polarization vector ($\mathcal{S}^\mu_{\text{accT}}$), gradient polarization vector of chemical potential with temperature ($\mathcal{S}^\mu_{\text{chemical}}$), and external electromagnetic field polarization ($\mathcal{S}^\mu_{\text{EB}}$). Usually, S^μ_{shear} and S^μ_{chemical} are also known as the Shear Induced Polarization (SIP) and the Spin Hall Effect (SHE). For detailed investigations of these polarization vectors, please see references [26,28,34,35,66–70]. Due to the rapid decay of the electromagnetic field and the lack of a good understanding of its profile in heavy-ion collisions, we consider only the first four terms while neglecting the contribution from $\mathcal{S}^\mu_{\text{EB}}$.

In the rest frame of Λ (or $\bar{\Lambda}$) baryons, the formula of spin polarization vector is

$$\vec{P}^*(\mathbf{p}) = \vec{P}(\mathbf{p}) - \frac{\vec{P}(\mathbf{p}) \cdot \vec{p}}{p^0(p^0 + m)}\vec{p}, \tag{19}$$

with

$$P^\mu(\mathbf{p}) \equiv \frac{1}{s}\mathcal{S}^\mu(\mathbf{p}), \tag{20}$$

where $s = 1/2$ represents the spin of the particle. Averaging its transverse momentum and rapidity, one can derive the local polarization of hyperons,

$$\langle\vec{P}(\phi_p)\rangle = \frac{\int_{y_{\min}}^{y_{\max}} dy \int_{p_{\mathrm{Tmin}}}^{p_{\mathrm{Tmax}}} p_{\mathrm{T}}dp_{\mathrm{T}}[\Phi(\mathbf{p})\vec{P}^*(\mathbf{p})]}{\int_{y_{\min}}^{y_{\max}} dy \int_{p_{\mathrm{Tmin}}}^{p_{\mathrm{Tmax}}} p_{\mathrm{T}}dp_{\mathrm{T}}\Phi(\mathbf{p})}. \tag{21}$$

Here, ϕ_p represents the azimuthal angle, $\Phi(\mathbf{p})$ is an integration on the freeze-out hypersurface defined in Equation (18). In this study, we set the masses of Λ and $\bar{\Lambda}$ hyperons to be $m = 1.116$ GeV. Finally, by performing azimuthal integration on Equation (21) and taking its $-\hat{y}$ component, the global polarization along the out-of-plane direction can be obtained. We have not taken into account the contributions to Λ hyperons polarization from resonance decays in this study, which can be incorporated based on Ref. [71] in future work.

3. Numerical Results

Our phenomenological study will first present the dependence of the global polarization of Λ and $\bar{\Lambda}$ hyperons on centrality, transverse momentum, and rapidity in 19.6 GeV Au+Au collisions. We then discuss how the magnitude of the net baryon density influences the splitting of the global polarization of hyperons. We close this section by performing the impact of the tilt geometry of the net baryon density on the global polarization splitting.

### 3.1. Global Polarization of Λ and $\bar{\Lambda}$ Hyperons

In Figure 2, we show the global polarization of Λ and $\bar{\Lambda}$ hyperons analyzed within transverse momentum $p_{\mathrm{T}} \in [0.5\,\text{GeV/c}, 3.0\,\text{GeV/c}]$ and rapidity $y \in [-1, 1]$ in 19.6 GeV Au+Au collisions. Because we have defined the $+x$ direction to align with the impact parameter, the global momentum is directed towards the negative y direction. Therefore, we present the global polarization along the out-of-plane direction ($-P^y$) in this and all subsequent figures. In the Figure 2 left plane, we compare different contributions, that is, different terms in Equation (17), as a function of collision centrality. It is observed that the spin polarization induced by the thermal vorticity plays a dominant contributor for both Λ and $\bar{\Lambda}$ hyperons polarization. As collision systems transition from central to non-central to peripheral, the splitting between the Λ and $\bar{\Lambda}$ hyperons increases. This behaviour is due to the tilted geometry of the net baryon density and a finite baryon chemical potential μ_B [21,36,45], with the splitting of global polarization ranging from zero in the most central collisions to 0.3% in peripheral collisions. In the Figure 2 right plane, we present the sum of the four spin polarization vectors of Λ and $\bar{\Lambda}$ hyperons (Total = thermal + shear + accT + chemical) and compared the results with experimental data. One finds that our calculation gives the same trend as the STAR experimental data from central to non-central collisions and a little bit underestimate for the experimental data at peripheral collision. One possible reason is the use of constant flow velocity gradient parameter f_v in this study [25]. We emphasize that the presence of a strong electromagnetic field will leas an increase of the splitting of global polarization [31].
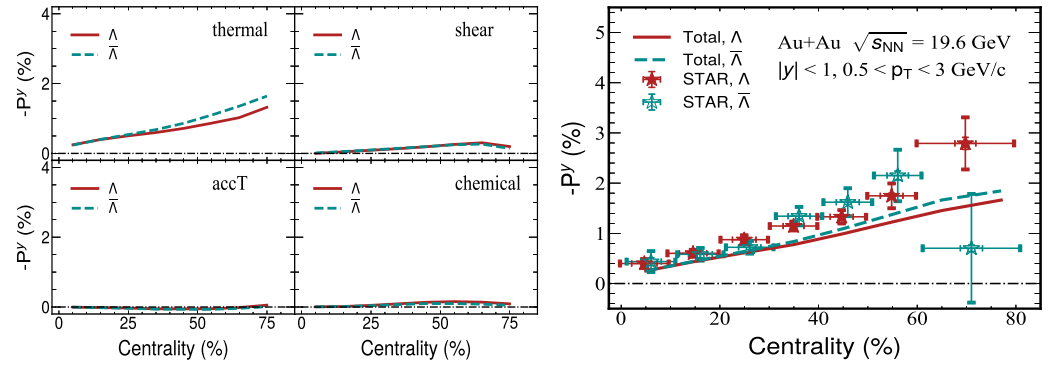
Figure 2. (Color online) The global polarization $-P^y$ of Λ and $\bar{\Lambda}$ hyperons as a function of centrality in Au+Au collisions at $\sqrt{s_{NN}} = 19.6$ GeV, analyzed within transverse momentum $p_T \in [0.5$ GeV/c, 3.0 GeV/c] and rapidity $y \in [-1, 1]$. Left plane: global polarization induced by different terms. Right: the global polarization of Λ and $\bar{\Lambda}$ (Total = thermal + shear + accT + chemical). The experimental data are from the RHIC-STAR Collaboration [20].

In Figure 3 left plane, we present the $-P^y$ of Λ and $\bar{\Lambda}$ hyperons as a function of transverse momentum p_T in 20–50% centrality Au+Au collisions. The rapidity region $|y| < 1$ of hyperons is used for the analysis. One observe that our model calculations, which combine the four contributions (labeled as "Total"), provide a satisfactory description of the Λ's (and $\bar{\Lambda}$'s) global polarization as compared to the STAR data [20]. A minor difference is observed between Λ and $\bar{\Lambda}$. Furthermore, the combination of thermal vorticity and shear tensor contributions results in a non-montonic p_T dependence of $-P^y$, due to their opposing effects [37]. This feature can be further investigated using more precise experimental data in the future.
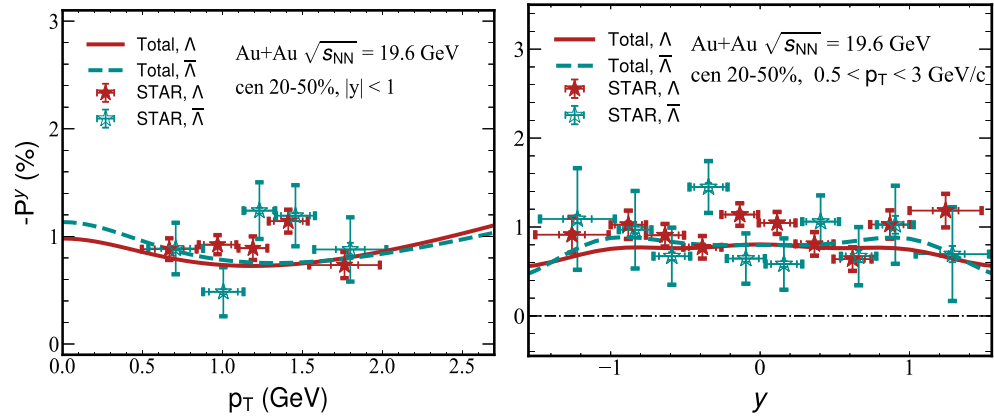
Figure 3. (Color online) The global polarization P^y of Λ and $\bar{\Lambda}$ as a function of transverse momentum p_T (**left**) and rapidity y (**right**) in 20–50% Au+Au collisions at $\sqrt{s_{NN}} = 19.6$ GeV, analyzed within $y \in [-1, 1]$ (**left**), $p_T \in [0.5$ GeV/c, 3 GeV/c] (**right**) and compared to the STAR data [20].

In Figure 3 right plane, we show the $-P^y$ as a function of rapidity y in 20–50% centrality Au+Au collisions within the transverse momentum region $p_T \in [0.5$ GeV/c, 3 GeV/c]. Our calculation gives a suitable estimation of the experimental measurements in rapidity region $y \in [-1.5, 1.5]$. The global polarization of $\bar{\Lambda}$ hyperons is a little bit larger than the Λ hyperons within rapidity greater than 0.5 in the forward and backward. We note here that the experimental data currently shown in Figure 3 have large uncertainly. Precise experimental measurements in the future, when compared to results in this study, may provide more constraints on the net baryon density distribution at the initial stage.

3.2. Effect of the Magnitude of the Net Baryon Density on the Global Polarization Splitting

After studying the global polarization of Λ and $\bar{\Lambda}$ hyperons, we now investigate the splitting of the global polarization $-P^y_{(\Lambda-\bar{\Lambda})}$ in Au+Au collisions at $\sqrt{s_{NN}} = 19.6$ GeV. We vary the magnitude of the net baryon density at the initial stage in Equation (7) to examine its impact on the splitting of the global polarization of Λ and $\bar{\Lambda}$ hyperons.

In the left plane of Figure 4, we present the $-P^y_{(\Lambda-\bar{\Lambda})}$ as a function of the transverse momentum p_T for different initial net baryon densities ($0.0n_0$, $0.5n_0$, $1.0n_0$, $1.5n_0$) in collision centrality 20–50%. One observes that when the net baryon density is zero (i.e., no net baryon density), the splitting of the global polarization $-P^y_{(\Lambda-\bar{\Lambda})}$ remains zero as the transverse momentum p_T increases. As the initial net baryon density increases, the value of splitting $-P^y_{(\Lambda-\bar{\Lambda})}$ also increases. One can observe that a higher magnitude of initial net baryon density leads to a larger splitting of the global polarization. The value of $-P^y_{(\Lambda-\bar{\Lambda})}$ for all cases crosses zero at a transverse momentum $p_T \approx 1.45$ GeV/c.
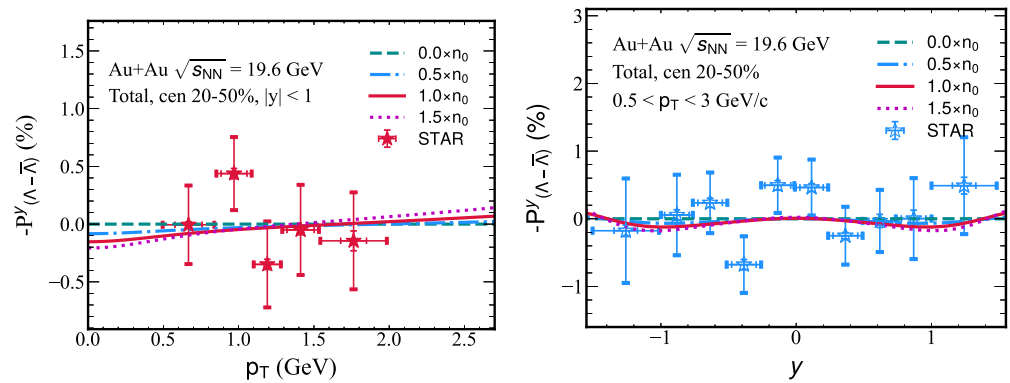
Figure 4. (Color online) The global polarization splitting $-P^y_{(\Lambda-\bar{\Lambda})}$ is studied as a function of transverse momentum P_T (**left**) and rapidity y (**right**) for different magnitudes of net baryon densities ($0.0n_0, 0.5n_0, 1.0n_0, 1.5n_0$) in Au+Au collisions at $\sqrt{s_{NN}} = 19.6$ GeV with centrality of 20–50%, analyzed within $y \in [-1,1]$ (**left**), $p_T \in [0.5 \text{ GeV/c}, 3.0 \text{ GeV/c}]$ (**right**) and compared to the STAR data [20].

In the right plane of Figure 4, we show $-P^y_{(\Lambda-\bar{\Lambda})}$ as a function of the rapidity y for a different initial net baryon density. One can see that when the initial net baryon density is zero, the global polarization splitting of hyperons remains zero with respect to rapidity y. As the magnitude of net baryon density increases, a slight change in the splitting of the global polarization can be observed at both the forward and backward rapidity regions. Our calculations tend to underestimate the experimental data, and the splitting of the global polarization is approximately zero at mid-rapidity regions for all four cases ($0.0n_0$, $0.5n_0$, $1.0n_0$, $1.5n_0$).

We find that both the $-P^y_{(\Lambda-\bar{\Lambda})}$. vs. p_T and $-P^y_{(\Lambda-\bar{\Lambda})}$. vs. y are non-zero when there is a non-zero net baryon density at the initial stage. Additionally, a larger net baryon density leads to a larger splitting of the global polarization. We emphasize that it is still difficult to determine the magnitude of the net baryon density based on the experimental data due to their large uncertainties. Further measurements may help to improve our understanding of the magnitude of the net baryon density in heavy ion collisions.

3.3. Effect of the Tilted Geometry of the Net Baryon Density on the Global Polarization Splitting

Now, we shift our focus to the effect of the tilted geometry of the net baryon density on the global polarization splitting of Λ and $\bar{\Lambda}$ hyperons in centrality 20–50% Au+Au collisions at $\sqrt{s_{NN}} = 19.6$ GeV.

In the left plane of Figure 5, we present the $-P^y_{(\Lambda-\bar{\Lambda})}$ as a function of the transverse momentum p_T in collision centrality 20–50% Au+Au collisions for a different longitudinal

tilted geometry of the net baryon densities (0.9 Ht, 1.0 Ht, 1.2 Ht, 1.5 Ht). We use the value of 1.2 Ht to indicate that the initial net baryon density is 1.2 times more tilted than the initial energy density. One can observe that when the net baryon density becomes more tilted, the global polarization splitting $-P^y_{(\Lambda-\bar{\Lambda})}$ increases from negative towards positive. We find that the global polarization splitting $-P^y_{(\Lambda-\bar{\Lambda})}$ .vs. p_T is very sensitive to the geometry of the net baryon density.
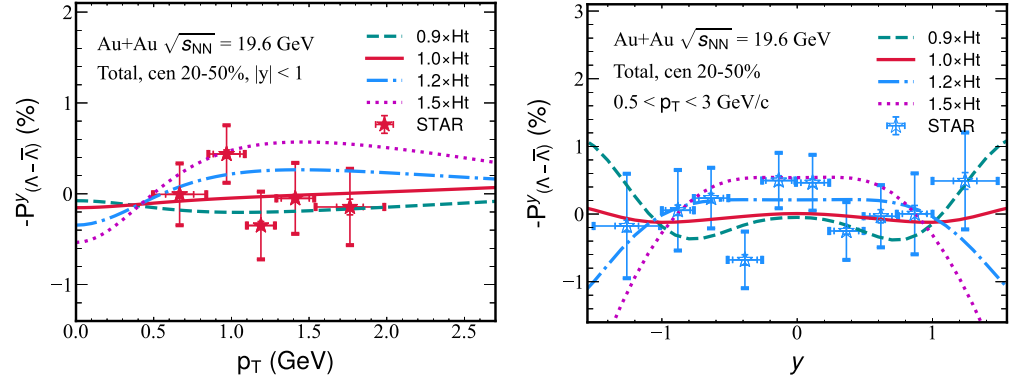
Figure 5. (Color online) The splitting of the global polarization $P^y_{(\Lambda-\bar{\Lambda})}$ as a function of transverse momentum p_T (**left**) and rapidity y (**right**) for different tilted geometry (0.9 Ht, 1.0 Ht, 1.2 Ht, 1.5 Ht) in 20–50% Au+Au collisions at $\sqrt{s_{NN}} = 19.6$ GeV, analyzed within $y \in [-1,1]$ (**left**), $p_T \in [0.5\,\mathrm{GeV}/c, 3.0\,\mathrm{GeV}/c]$ (**right**) and compared to the STAR data [20].

In the right plane of Figure 5, we show the $-P^y_{(\Lambda-\bar{\Lambda})}$ as a function of the rapidity y for a different longitudinal tilted geometry of the net baryon densities within transverse momentum $p_T \in [0.5\,\mathrm{GeV}/c, 3.0\,\mathrm{GeV}/c]$. One can find that when the net bayon density becomes more tilted, the value of the global polarization splitting of hyperons increases from negative to positive. Contrary to the impact of the net baryon density magnitude, a more tilted geometry of net baryon density results in a greater separation of the global polarization of Λ and $\bar{\Lambda}$ hyperons in the mid-rapidity and forward/backward rapidity regions. Due to the large uncertainties present in experimental data, additional measurements could help to enhance our understanding of both the magnitude and geometry of the initial net baryon density.

4. Conclusions

In this work, we used the viscous hydrodynamic model CLVisc with a modified 3D optical Glauber model initial condition to study the hyperon spin polarization in Au+Au collisions at $\sqrt{s_{NN}} = 19.6$ GeV. With a finite net baryon density, our hydrodynamic model nicely describes the global polarization $-P^y$ of Λ and $\bar{\Lambda}$ hyperons as a function of centrality, transverse momentum, and rapidity.

With CLVisc hydrodynamic simulation, we study how the net baryon density influence the global polarization splitting of Λ and $\bar{\Lambda}$ hyperons. We find that the global polarization splitting shows strong sensitivities to both the magnitude and tilted geometry of the net baryon density. In the meantime, we observe that the tilted geometry of the net baryon density has a greater influence on $-P^y_{(\Lambda-\bar{\Lambda})}(p_T)$ and $-P^y_{(\Lambda-\bar{\Lambda})}(y)$ compared to its magnitude. Therefore, the global polarization of Λ and $\bar{\Lambda}$ hyperons could serve as a robust and promising observable for studying the properties of the baryon density in heavy ion collision at RHIC-BES (Beam Energy Scan) energies. Due to the inconspicuous splitting behavior observed in many other experimental data above 19.6 GeV and the lack of data below 19.6 GeV, we chose to focus our study on 19.6 GeV and did not include comparisons with results at other energies in this work. In our future study, we will explore the splitting behavior at energy range below 19.6 GeV. We also note that utilizing a uniform distribution of nucleon density yields polarization results that are not substantially

dissimilar to those acquired through the Wood–Saxon distribution [58]. Additionally, since the global polarization is currently constrained to contributions from primary Λ particles, the effects of hadronic scatterings after the QGP phase have not been included in the present work. This limitation results in a degree of uncertainty in our current calculations. The impacts of hadron scattering and resonance decay on the polarization of Λ hyperons will be explored in our upcoming efforts. Future studies will include more precise measurements, the spin polarization observables [33,72–74], in conjunction with the QGP anisotropic flow observables [75], and will provide strong constraints on the 3-dimensional dynamics (e.g., electromagnetic field [76]) of the hot and dense QGP formed in heavy-ion collisions.

Author Contributions: Conceptualization, Z.J., S.Y. and X.Y.; methodology, S.Y., X.Y. and Z.J.; software, Z.J.; validation, S.Y. and X.Y.; formal analysis, S.Y. and Z.J.; investigation, S.Y. and X.Y.; data curation, Z.J.; writing—original draft preparation, S.Y. and X.Y.; writing—review and editing, Z.J.; supervision, Z.J.; project administration, Z.J.; funding acquisition, Z.J. All authors have read and agreed to the published version of the manuscript.

Data Availability Statement: The data presented in this study are available on request from the corresponding author.

Conflicts of Interest: The authors declare no conflict of interest.

References

1. Ollitrault, J.Y. Anisotropy as a signature of transverse collective flow. *Phys. Rev. D* **1992**, *46*, 229–245. [CrossRef] [PubMed]
2. Rischke, D.H.; Bernard, S.; Maruhn, J.A. Relativistic hydrodynamics for heavy ion collisions. 1. General aspects and expansion into vacuum. *Nucl. Phys. A* **1995**, *595*, 346–382. [CrossRef]
3. Sorge, H. Elliptical flow: A Signature for early pressure in ultrarelativistic nucleus–nucleus collisions. *Phys. Rev. Lett.* **1997**, *78*, 2309–2312. [CrossRef]
4. Bass, S.; Gyulassy, M.; Stoecker, H.; Greiner, W. Signatures of quark gluon plasma formation in high-energy heavy ion collisions: A Critical review. *J. Phys. G* **1999**, *25*, R1–R57. [CrossRef]
5. Aguiar, C.E.; Hama, Y.; Kodama, T.; Osada, T. Event-by-event fluctuations in hydrodynamical description of heavy ion collisions. *Nucl. Phys. A* **2002**, *698*, 639–642. [CrossRef]
6. Shuryak, E. Why does the quark gluon plasma at RHIC behave as a nearly ideal fluid? *Prog. Part. Nucl. Phys.* **2004**, *53*, 273–303. [CrossRef]
7. Heinz, U.; Snellings, R. Collective flow and viscosity in relativistic heavy-ion collisions. *Ann. Rev. Nucl. Part. Sci.* **2013**, *63*, 123–151. [CrossRef]
8. Busza, W.; Rajagopal, K.; van der Schee, W. Heavy Ion Collisions: The Big Picture, and the Big Questions. *Ann. Rev. Nucl. Part. Sci.* **2018**, *68*, 339–376. [CrossRef]
9. Aoki, Y.; Endrodi, G.; Fodor, Z.; Katz, S.D.; Szabo, K.K. The Order of the quantum chromodynamics transition predicted by the standard model of particle physics. *Nature* **2006**, *443*, 675–678. [CrossRef]
10. Becattini, F.; Piccinini, F.; Rizzo, J. Angular momentum conservation in heavy ion collisions at very high energy. *Phys. Rev. C* **2008**, *77*, 024906. [CrossRef]
11. Becattini, F.; Piccinini, F. The Ideal relativistic spinning gas: Polarization and spectra. *Ann. Phys.* **2008**, *323*, 2452–2473. [CrossRef]
12. Liang, Z.T.; Wang, X.N. Globally polarized quark–gluon plasma in non-central A+A collisions. *Phys. Rev. Lett.* **2005**, *94*, 102301; Erratum: *Phys. Rev. Lett.* **2006**, *96*, 039901. [CrossRef] [PubMed]
13. Liang, Z.T.; Wang, X.N. Spin alignment of vector mesons in non-central A+A collisions. *Phys. Lett. B* **2005**, *629*, 20–26. [CrossRef]
14. Betz, B.; Gyulassy, M.; Torrieri, G. Polarization probes of vorticity in heavy ion collisions. *Phys. Rev. C* **2007**, *76*, 044901. [CrossRef]
15. Gao, J.H.; Chen, S.W.; Deng, W.t.; Liang, Z.T.; Wang, Q.; Wang, X.N. Global quark polarization in non-central A+A collisions. *Phys. Rev. C* **2008**, *77*, 044902. [CrossRef]
16. Chen, S.w.; Deng, J.; Gao, J.h.; Wang, Q. A General derivation of differential cross-section in quark-quark scatterings at fixed impact parameter. *Front. Phys. China* **2009**, *4*, 509–516. [CrossRef]
17. Huang, X.G.; Huovinen, P.; Wang, X.N. Quark Polarization in a Viscous quark–gluon Plasma. *Phys. Rev. C* **2011**, *84*, 054910. [CrossRef]

18. Adamczyk, L.; Adkins, J.K.; Agakishiev, G.; Aggarwal, M.M.; Ahammed, Z.; Ajitanand, N.N.; Alekseev, I.; Anderson, D.M.; Aoyama, R.; Aparin, A.; et al. Global Λ hyperon polarization in nuclear collisions: Evidence for the most vortical fluid. *Nature* **2017**, *548*, 62–65. [CrossRef]

19. Adam, J.; Adamczyk, L.; Adams, J.R.; Adkins, J.K.; Agakishiev, G.; Aggarwal, M.M.; Ahammed, Z.; Alekseev, I.; Anderson, D.M.; Aoyama, R.; et al. Polarization of Λ ($\bar{\Lambda}$) hyperons along the beam direction in Au+Au collisions at $\sqrt{s_{NN}}$ = 200 GeV. *Phys. Rev. Lett.* **2019**, *123*, 132301. [CrossRef]

20. Abdulhamid, M.I.; Aboona, B.E.; Adam, J.; Adamczyk, L.; Adams, J.R.; Aggarwal, I.; Aggarwal, M.M.; Ahammed, Z.; Alpatov, E.; Anderson, D.M.; et al. Global polarization of Λ and Λ^{-} hyperons in Au+Au collisions at $\sqrt{s_{NN}}$ = 19.6 and 27 GeV. *Phys. Rev. C* **2023**, *108*, 014910. [CrossRef]

21. Fu, B.; Xu, K.; Huang, X.G.; Song, H. Hydrodynamic study of hyperon spin polarization in relativistic heavy ion collisions. *Phys. Rev. C* **2021**, *103*, 024903. [CrossRef]

22. Ivanov, Y.B.; Toneev, V.D.; Soldatov, A.A. Estimates of hyperon polarization in heavy-ion collisions at collision energies $\sqrt{s_{NN}}$ = 4–40 GeV. *Phys. Rev. C* **2019**, *100*, 014908. [CrossRef]

23. Ivanov, Y.B. Global Λ polarization in moderately relativistic nuclear collisions. *Phys. Rev. C* **2021**, *103*, L031903. [CrossRef]

24. Wu, H.Z.; Pang, L.G.; Huang, X.G.; Wang, Q. Local spin polarization in high energy heavy ion collisions. *Phys. Rev. Res.* **2019**, *1*, 033058. [CrossRef]

25. Ryu, S.; Jupic, V.; Shen, C. Probing early-time longitudinal dynamics with the Λ hyperon's spin polarization in relativistic heavy-ion collisions. *Phys. Rev. C* **2021**, *104*, 054908. [CrossRef]

26. Yi, C.; Pu, S.; Yang, D.L. Reexamination of local spin polarization beyond global equilibrium in relativistic heavy ion collisions. *Phys. Rev. C* **2021**, *104*, 064901. [CrossRef]

27. Alzhrani, S.; Ryu, S.; Shen, C. Λ spin polarization in event-by-event relativistic heavy-ion collisions. *Phys. Rev. C* **2022**, *106*, 014905. [CrossRef]

28. Wu, X.Y.; Yi, C.; Qin, G.Y.; Pu, S. Local and global polarization of Λ hyperons across RHIC-BES energies: The roles of spin hall effect, initial condition, and baryon diffusion. *Phys. Rev. C* **2022**, *105*, 064909. [CrossRef]

29. Xia, X.L.; Li, H.; Tang, Z.B.; Wang, Q. Probing vorticity structure in heavy-ion collisions by local Λ polarization. *Phys. Rev. C* **2018**, *98*, 024905. [CrossRef]

30. Wei, D.X.; Deng, W.T.; Huang, X.G. Thermal vorticity and spin polarization in heavy-ion collisions. *Phys. Rev. C* **2019**, *99*, 014905. [CrossRef]

31. Guo, Y.; Shi, S.; Feng, S.; Liao, J. Magnetic Field Induced Polarization Difference between Hyperons and Anti-hyperons. *Phys. Lett. B* **2019**, *798*, 134929. [CrossRef]

32. Li, H.; Pang, L.G.; Wang, Q.; Xia, X.L. Global Λ polarization in heavy-ion collisions from a transport model. *Phys. Rev. C* **2017**, *96*, 054908. [CrossRef]

33. Abdallah, M.S.; Aboona, B.E.; Adam, J.; Adamczyk, L.; Adams, J.R.; Adkins, J.K.; Agakishiev, G.; Aggarwal, I.; Aggarwal, M.M.; Ahammed, Z.; et al. Pattern of global spin alignment of ϕ and K^{*0} mesons in heavy-ion collisions. *Nature* **2023**, *614*, 244–248. [CrossRef]

34. Liu, S.Y.F.; Yin, Y. Spin Hall effect in heavy-ion collisions. *Phys. Rev. D* **2021**, *104*, 054043. [CrossRef]

35. Fu, B.; Pang, L.; Song, H.; Yin, Y. Signatures of the spin Hall effect in hot and dense QCD matter. *arXiv* **2022**, arXiv:2201.12970.

36. Jiang, Z.F.; Wu, X.Y.; Cao, S.; Zhang, B.W. Directed flow and global polarization in Au+Au collisions across energies covered by the beam energy scan at RHIC. *Phys. Rev. C* **2023**, *107*, 034904. [CrossRef]

37. Jiang, Z.F.; Wu, X.Y.; Cao, S.; Zhang, B.W. Hyperon polarization and its relation with directed flow in high-energy nuclear collisions. *Phys. Rev.* **2023**, *108*, 064904. [CrossRef]

38. Pang, L.G.; Hatta, Y.; Wang, X.N.; Xiao, B.W. Analytical and numerical Gubser solutions of the second-order hydrodynamics. *Phys. Rev. D* **2015**, *91*, 074027. [CrossRef]

39. Pang, L.G.; Petersen, H.; Wang, X.N. Pseudorapidity distribution and decorrelation of anisotropic flow within the open-computing-language implementation CLVisc hydrodynamics. *Phys. Rev. C* **2018**, *97*, 064918. [CrossRef]

40. Wu, X.Y.; Pang, L.G.; Qin, G.Y.; Wang, X.N. Longitudinal fluctuations and decorrelations of anisotropic flows at energies available at the CERN Large Hadron Collider and at the BNL Relativistic Heavy Ion Collider. *Phys. Rev. C* **2018**, *98*, 024913. [CrossRef]

41. Wu, X.Y.; Qin, G.Y.; Pang, L.G.; Wang, X.N. (3+1)-D viscous hydrodynamics at finite net baryon density: Identified particle spectra, anisotropic flows, and flow fluctuations across energies relevant to the beam-energy scan at RHIC. *Phys. Rev. C* **2022**, *105*, 034909. [CrossRef]

42. Wu, J.; Cao, S.; Li, F. Partonic Critical Opalescence and Its Impact on the Jet Quenching Parameter $\hat{q}$. *arXiv* **2022**, arXiv:2208.14297.

43. Zhao, W.; Ke, W.; Chen, W.; Luo, T.; Wang, X.N. From Hydrodynamics to Jet Quenching, Coalescence, and Hadron Cascade: A Coupled Approach to Solving the RAA⊗v2 Puzzle. *Phys. Rev. Lett.* **2022**, *128*, 022302. [CrossRef]

44. Vitiuk, O.; Bravina, L.V.; Zabrodin, E.E. Is different Λ and $\bar{\Lambda}$ polarization caused by different spatio-temporal freeze-out picture? *Phys. Lett. B* **2020**, *803*, 135298. [CrossRef]

45. Cimerman, J.; Karpenko, I.; Tomasik, B.; Huovinen, P. Next-generation multifluid hydrodynamic model for nuclear collisions at sNN from a few GeV to a hundred GeV. *Phys. Rev. C* **2023**, *107*, 044902. [CrossRef]

46. Loizides, C.; Kamin, J.; d'Enterria, D. Improved Monte Carlo Glauber predictions at present and future nuclear colliders. *Phys. Rev. C* **2018**, *97*, 054910; Erratum: *Phys. Rev. C* **2019**, *99*, 019901. [CrossRef]

47. Jiang, Z.F.; Yang, C.B.; Peng, Q. Directed flow of charged particles within idealized viscous hydrodynamics at energies available at the BNL Relativistic Heavy Ion Collider and at the CERN Large Hadron Collider. *Phys. Rev. C* **2021**, *104*, 064903. [CrossRef]
48. Jiang, Z.F.; Cao, S.; Wu, X.Y.; Yang, C.B.; Zhang, B.W. Longitudinal distribution of initial energy density and directed flow of charged particles in relativistic heavy-ion collisions. *Phys. Rev. C* **2022**, *105*, 034901. [CrossRef]
49. Jiang, Z.F.; Cao, S.; Xing, W.J.; Wu, X.Y.; Yang, C.B.; Zhang, B.W. Probing the initial longitudinal density profile and electromagnetic field in ultrarelativistic heavy-ion collisions with heavy quarks. *Phys. Rev. C* **2022**, *105*, 054907. [CrossRef]
50. Bozek, P.; Wyskiel, I. Directed flow in ultrarelativistic heavy-ion collisions. *Phys. Rev. C* **2010**, *81*, 054902. [CrossRef]
51. Bozek, P. Flow and interferometry in 3+1 dimensional viscous hydrodynamics. *Phys. Rev. C* **2012**, *85*, 034901. [CrossRef]
52. Pang, L.G.; Endrődi, G.; Petersen, H. Magnetic-field-induced squeezing effect at energies available at the BNL Relativistic Heavy Ion Collider and at the CERN Large Hadron Collider. *Phys. Rev. C* **2016**, *93*, 044919. [CrossRef]
53. Denicol, G.S.; Gale, C.; Jeon, S.; Monnai, A.; Schenke, B.; Shen, C. Net baryon diffusion in fluid dynamic simulations of relativistic heavy-ion collisions. *Phys. Rev. C* **2018**, *98*, 034916. [CrossRef]
54. Bozek, P. Splitting of proton-antiproton directed flow in relativistic heavy-ion collisions. *Phys. Rev. C* **2022**, *106*, L061901. [CrossRef]
55. Shen, C.; Schenke, B. Dynamical initial state model for relativistic heavy-ion collisions. *Phys. Rev. C* **2018**, *97*, 024907. [CrossRef]
56. Bialas, A.; Jezabek, M. Bremsstrahlung from color charges as a source of soft particle production in hadronic collisions. *Phys. Lett. B* **2004**, *590*, 233–238. [CrossRef]
57. Shen, C.; Alzhrani, S. Collision-geometry-based 3D initial condition for relativistic heavy-ion collisions. *Phys. Rev. C* **2020**, *102*, 014909. [CrossRef]
58. Li, X.; Jiang, Z.F.; Cao, S.; Deng, J. Evolution of global polarization in relativistic heavy-ion collisions within a perturbative approach. *Eur. Phys. J. C* **2023**, *83*, 96. [CrossRef]
59. Jeżabek, M.; Rybicki, A. Baryon number in proton-proton and proton-nucleus high energy collisions. *Eur. Phys. J. Plus* **2021**, *136*. [CrossRef]
60. Akamatsu, Y.; Asakawa, M.; Hirano, T.; Kitazawa, M.; Morita, K.; Murase, K.; Nara, Y.; Nonaka, C.; Ohnishi, A. Dynamically integrated transport approach for heavy-ion collisions at high baryon density. *Phys. Rev. C* **2018**, *98*, 024909. [CrossRef]
61. Monnai, A.; Schenke, B.; Shen, C. Equation of state at finite densities for QCD matter in nuclear collisions. *Phys. Rev. C* **2019**, *100*, 024907. [CrossRef]
62. Monnai, A.; Schenke, B.; Shen, C. QCD Equation of State at Finite Chemical Potentials for Relativistic Nuclear Collisions. *Int. J. Mod. Phys. A* **2021**, *36*, 2130007. [CrossRef]
63. Becattini, F.; Chandra, V.; Del Zanna, L.; Grossi, E. Relativistic distribution function for particles with spin at local thermodynamical equilibrium. *Ann. Phys.* **2013**, *338*, 32–49. [CrossRef]
64. Fang, R.-h.; Pang, L.-g.; Wang, Q.; Wang, X.-n. Polarization of massive fermions in a vortical fluid. *Phys. Rev. C* **2016**, *94*, 024904. [CrossRef]
65. Karpenko, I.; Becattini, F. Lambda polarization in heavy ion collisions: From RHIC BES to LHC energies. *Nucl. Phys. A* **2019**, *982*, 519–522. [CrossRef]
66. Hidaka, Y.; Pu, S.; Yang, D.L. Nonlinear Responses of Chiral Fluids from Kinetic Theory. *Phys. Rev. D* **2018**, *97*, 016004. [CrossRef]
67. Yi, C.; Pu, S.; Gao, J.H.; Yang, D.L. Hydrodynamic helicity polarization in relativistic heavy ion collisions. *Phys. Rev. C* **2022**, *105*, 044911. [CrossRef]
68. Becattini, F.; Buzzegoli, M.; Palermo, A. Spin-thermal shear coupling in a relativistic fluid. *Phys. Lett. B* **2021**, *820*, 136519. [CrossRef]
69. Liu, S.Y.F.; Yin, Y. Spin polarization induced by the hydrodynamic gradients. *J. High Energy Phys.* **2021**, *2021*, 188. [CrossRef]
70. Fu, B.; Liu, S.Y.F.; Pang, L.; Song, H.; Yin, Y. Shear-Induced Spin Polarization in Heavy-Ion Collisions. *Phys. Rev. Lett.* **2021**, *127*, 142301. [CrossRef]
71. Becattini, F.; Karpenko, I.; Lisa, M.; Upsal, I.; Voloshin, S. Global hyperon polarization at local thermodynamic equilibrium with vorticity, magnetic field and feed-down. *Phys. Rev. C* **2017**, *95*, 054902. [CrossRef]
72. Huang, X.G. Vorticity and Spin Polarization—A Theoretical Perspective. *Nucl. Phys. A* **2021**, *1005*, 121752. [CrossRef]
73. Serenone, W.M.; Barbon, J.G.P.; Chinellato, D.D.; Lisa, M.A.; Shen, C.; Takahashi, J.; Torrieri, G. Λ polarization from thermalized jet energy. *Phys. Lett. B* **2021**, *820*, 136500. [CrossRef]
74. Sheng, X.L.; Oliva, L.; Liang, Z.T.; Wang, Q.; Wang, X.N. Spin Alignment of Vector Mesons in Heavy-Ion Collisions. *Phys. Rev. Lett.* **2023**, *131*, 042304. [CrossRef]
75. Harris, J.W.; Müller, B. "QGP Signatures" Revisited. *arXiv* **2023**, arXiv:2308.05743.
76. Huang, A.; She, D.; Shi, S.; Huang, M.; Liao, J. Dynamical magnetic fields in heavy-ion collisions. *Phys. Rev. C* **2023**, *107*, 034901. [CrossRef]